

LETTER • OPEN ACCESS

Ultra-long wavelength Dirac plasmons in graphene capacitors

To cite this article: H Graef *et al* 2018 *J. Phys. Mater.* 1 01LT02

View the [article online](#) for updates and enhancements.



LETTER

Ultra-long wavelength Dirac plasmons in graphene capacitors

OPEN ACCESS

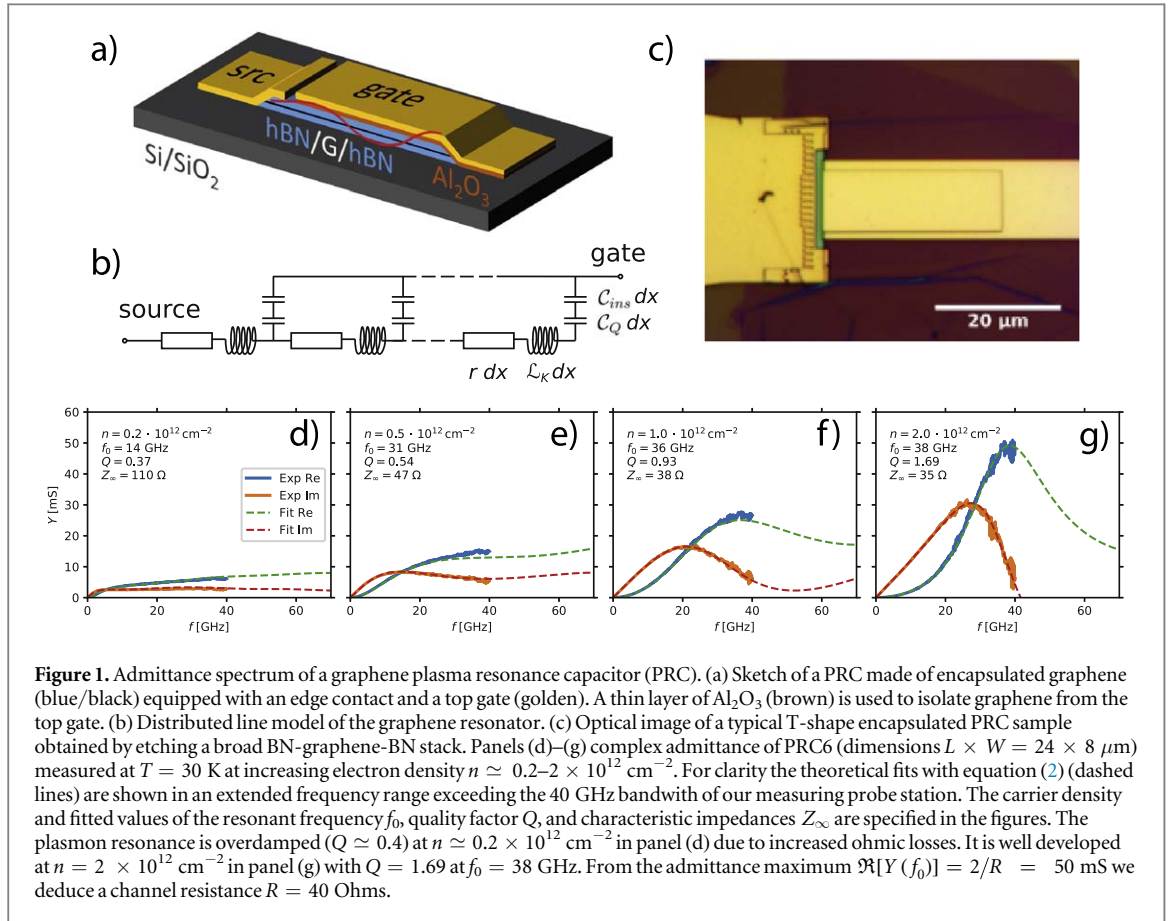
RECEIVED
22 June 2018ACCEPTED FOR PUBLICATION
29 August 2018PUBLISHED
17 September 2018Original content from this work may be used under the terms of the [Creative Commons Attribution 3.0 licence](#).

Any further distribution of this work must maintain attribution to the author(s) and the title of the work, journal citation and DOI.

H Graef^{1,2,5} , D Mele¹ , M Rosticher¹, L Banszerus³ , C Stampfer³ , T Taniguchi⁴ , K Watanabe⁴ , E Bocquillon¹ , G Fève¹ , J-M Berroir¹ , E H T Teo^{5,6} and B Plaçais¹ ¹ Laboratoire Pierre Aigrain, Ecole Normale Supérieure, PSL University, Sorbonne Université, Université Paris Diderot, Sorbonne Paris Cité, CNRS, 24 rue Lhomond, F-75005 Paris, France² CINTRA, UMI 3288, CNRS/NTU/Thales, Research Techno Plaza, 50 Nanyang Drive, 637553, Singapore³ JARA-FIT and 2nd Institute of Physics, RWTH Aachen University, D-52056 Aachen, Germany⁴ Advanced Materials Laboratory, National Institute for Materials Science, Tsukuba, Ibaraki 305-0047, Japan⁵ School of Electrical and Electronic Engineering, Nanyang Technological University, 50 Nanyang Avenue, Singapore 639798, Singapore⁶ School of Materials Science and Engineering, Nanyang Technological University, 50 Nanyang Avenue, Singapore 639798, SingaporeE-mail: bernard.placais@lpa.ens.fr**Keywords:** graphene, plasmonics, high-frequency transport, plasma resonance**Abstract**

Graphene is a valuable 2D platform for plasmonics as illustrated in recent THz and mid-infrared optics experiments. These high-energy plasmons however, couple to the dielectric surface modes giving rise to hybrid plasmon-polariton excitations. Ultra-long wavelengths address the low energy end of the plasmon spectrum, in the GHz–THz electronic domain, where intrinsic graphene Dirac plasmons are essentially decoupled from their environment. However experiments are elusive due to the damping by ohmic losses at low frequencies. We demonstrate here a plasma resonance capacitor (PRC) using hexagonal boron-nitride (hBN) encapsulated graphene at cryogenic temperatures in the near-ballistic regime. We report on a 100 μm quarter-wave plasmon mode, at 40 GHz, with a quality factor $Q \simeq 2$. The accuracy of the resonant technique yields a precise determination of the electronic compressibility and kinetic inductance, allowing to assess residual deviations from intrinsic Dirac plasmonics. Our GHz frequency capacitor experiment constitutes a first step towards the demonstration of plasma resonance transistors for microwave detection in the sub-THz domain for wireless communication and sensing. It also paves the way to the realization of doping-modulated superlattices where plasmon propagation is controlled by Klein tunneling.

Two-dimensional electron systems (2DES) sustain both single-particle and collective low-energy excitations, the latter being called plasmons. In graphene, their interplay is controlled by the electron density n which rules the kinetic energy, interactions and damping. Free 2DES plasmons are dispersive with $\omega_p \propto \sqrt{q}$ and a velocity v_p diverging in the long wavelength limit [1]. However, in the presence of a gate electrode, plasmons are screened in the long wavelength limit $\lambda_p \gtrsim d$ [2], where d is the gate-2DES distance, and acquire an energy-independent velocity $v_p = v_F \sqrt{(e^2 d / \pi \epsilon) (k_F / \hbar v_F)}$, where v_F and $k_F = \sqrt{\pi n}$ are the Fermi velocity and wave vector, and $\epsilon \simeq 3\epsilon_0$ is the hBN permittivity. Graphene plasmons have been mostly investigated in the THz and mid-infrared (MIR) optics domains where the damping length $\alpha^{-1} \gtrsim 10 \mu\text{m}$ was found to widely exceed the wavelength $\lambda_p \lesssim 1 \mu\text{m}$ [3–6]. In this high-energy range, plasmons couple to the dielectric surface modes, forming plasmon-polaritons states [5]. Ultra-long-wavelength plasmons ($\lambda_p \sim 100 \mu\text{m}$) belong to the GHz domain and do not suffer from this hybridization. They have been observed in high-mobility 2DESs in [2], but remain elusive in graphene in spite of the interest of manipulating collective chiral Dirac fermion excitations. A constitutive element of plasmon propagation is the kinetic inductance which has been measured in [7]. High-mobility graphene [8] offers the opportunity to investigate GHz plasmonics with a transport approach. Motivations are manifold; they include the demonstration of GHz plasma resonance devices [9], the investigation of plasmonic crystals in doping-modulated structures [10], that of interactions including viscous fluid effects at high temperatures [11, 12], or the coupling with hyperbolic phonon polaritons of the hBN dielectric [5, 13, 14] at high bias. In this letter, we demonstrate a plasma resonance capacitor (PRC in figure 1(a)) where 100 μm Dirac



plasmons propagate along a hBN-graphene-hBN-metal strip line of length $L \simeq 24 \mu\text{m}$ and aspect ratio $L/W = 3$ (figure 1(c)). We report on the fundamental mode, which is a quarter-wave resonance at $f_0 = v_p/4L \sim 40 \text{ GHz}$, where we achieve a quality factor $Q \simeq 2$ at low temperatures ($T = 10 \text{ K}$) corresponding to a damping length $\alpha^{-1} = 2QL/\pi \sim 30 \mu\text{m}$.

Our graphene resonator is a T-shape hBN-encapsulated single-layer graphene sample covered by a top metallization serving both as radio-frequency (RF) port and DC gate (see methods, figures 1(c) and 3). We have measured a series of eight devices, using both exfoliated and CVD graphene, but the results presented below focus on sample PRC6 ($L \times W = 24 \times 8 \mu\text{m}$) which has the highest mobility and largest quality factors. The device is embedded in a coplanar waveguide (CPW) and its RF gate-source admittance $Y(f, n, T)$ is measured in the range $f = 0\text{--}40 \text{ GHz}$, $n = 0\text{--}2 \times 10^{12} \text{ cm}^{-2}$ and $T = 10\text{--}300 \text{ K}$ using standard vector-network-analyzer (VNA) techniques (see methods and [15]). The strip line access, which has a broader width, constitutes the device source. It is equipped with a low-resistance edge contact (figure 1(c)). The source end of the strip is an impedance short, securing a plasmon node, the open end of the strip being an antinode so that the PRC sustains odd harmonics of the fundamental mode $f_0 = v_p/4L$.

We describe propagation by a distributed-line model (figure 1(b)). The line capacitance \mathcal{C} is the series addition of the insulator capacitance $C_{ins} = \epsilon W/d$ and the quantum capacitance $\mathcal{C}_Q = \frac{4e^2}{h} \frac{k_F W}{v_F}$ (low temperature). The large top-gate capacitance enhances the \mathcal{C}_Q contribution and gives access to a capacitance spectroscopy which is used below to determine the Dirac-point position. The line inductance is dominated by the kinetic contribution, which at low temperatures writes [7]

$$\mathcal{L}_K = \frac{h}{4e^2} \frac{2}{k_F v_F W}. \quad (1)$$

From these expressions one recovers the plasmon velocity $v_p = 1/\sqrt{\mathcal{L}_K \mathcal{C}}$ and the characteristic impedance $Z_\infty = \sqrt{\mathcal{L}_K/\mathcal{C}}$ of the plasmonic strip line. The line resistance $r = R/L$ accounts for plasmon losses which in principle include ohmic, viscous and dielectric contributions. The latter are negligible in our low-frequency range and viscous losses are minimized by using a plane wave geometry. Upon increasing the carrier density, the plasmonic response, with $\mathcal{L}_K \propto 1/k_F$ (single layer graphene), takes over single particle diffusive response, with $r \propto 1/k_F^2$ (constant mobility), allowing for low-damping plasmon propagation. The crossover occurs whenever the total strip resistance $R \lesssim Z_\infty$, or equivalently the plasmon damping length $\alpha^{-1} \gtrsim L$. Dealing with a resonant

device, the PRC admittance, $Y = j\mathcal{C}\omega \times \tanh \left[L\sqrt{j\mathcal{C}\omega(r + j\mathcal{L}_K\omega)} \right] / \sqrt{j\mathcal{C}\omega(r + j\mathcal{L}_K\omega)}$ [16], is conveniently cast into the compact form:

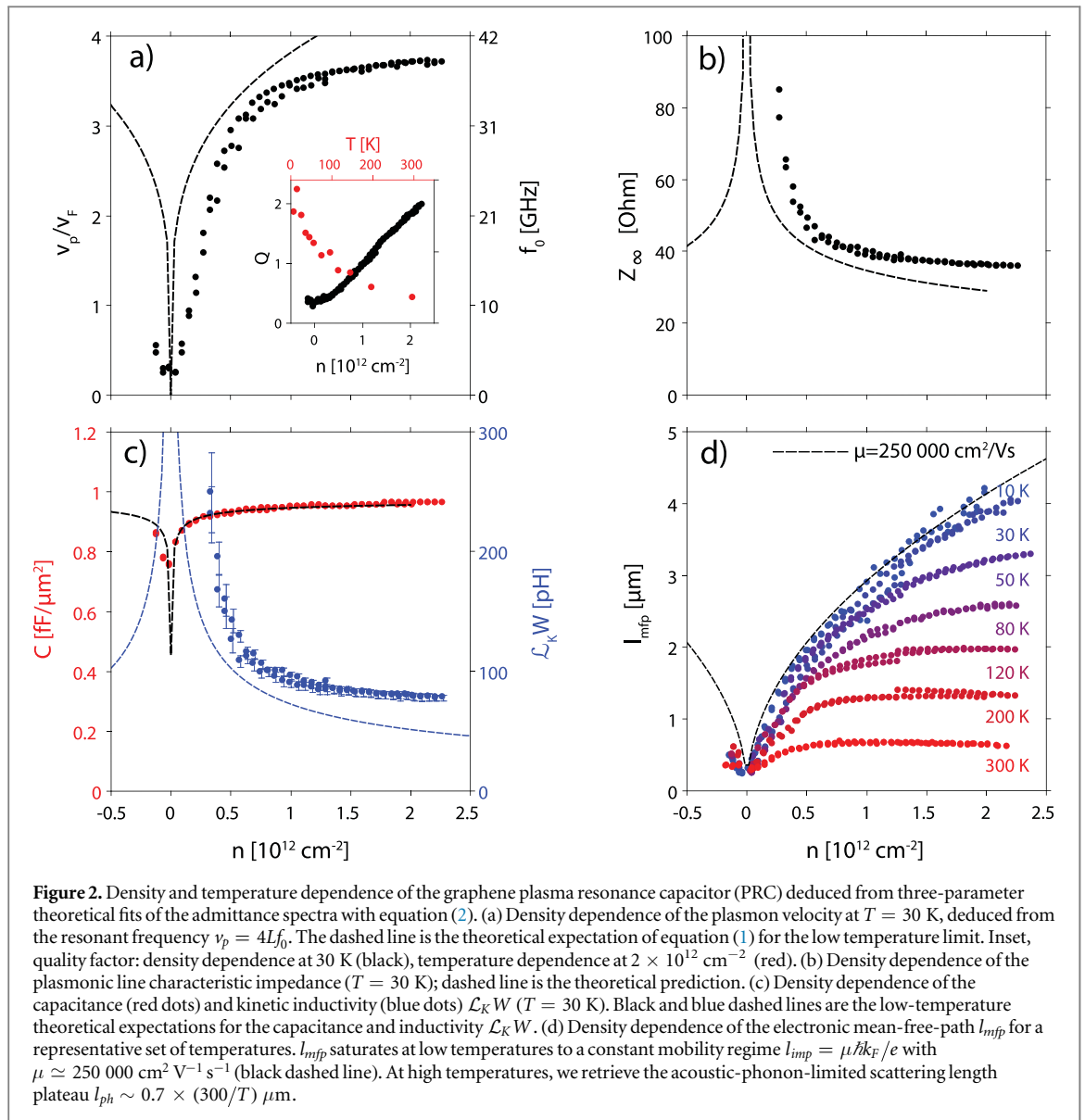
$$Y = Z_\infty^{-1} \times \frac{\tan(\tilde{f}\sqrt{1 - 2j/Q\tilde{f}})}{\sqrt{1 - 2j/Q\tilde{f}}}, \quad (2)$$

where $\tilde{f} = \omega L\sqrt{\mathcal{C}\mathcal{L}_K} = (\pi f)/(2f_0)$ is the reduced frequency. The capacitive character of the resonator is encoded in the low-frequency response $Y/L = j\mathcal{C}\omega$. Equation (2) features a resonance behavior with a fundamental frequency at $\tilde{f}_0 = \pi/2$, an admittance peak amplitude $\Re[Y(f_0)] = Q/Z_\infty = 2/R$ and a width $\Delta f \simeq f_0/Q$. It includes higher harmonics, constituting the frequency comb $f_k = (2k + 1)f_0$ with $Q_k \sim (2k + 1)Q$. The latter are discarded here due to the finite 40 GHz bandwidth of our cryogenic setup.

The rise of a plasma resonance in increasing electron density is illustrated in figures 1(d)–(g). Admittance spectra, measured at $T = 30$ K, have been obtained after deembedding a contact resistance $R_c = 43$ Ohms. Such a low value was obtained by back-gating the capacitor access region. Data are presented together with their fits with equation (2) (dashed lines). At the lowest density the channel resistance takes over the kinetic inductance. The plasmon resonance $f_0 \sim 14$ GHz is overdamped with $Q \sim 0.4$ (figure 1(d)). The admittance spectrum is reminiscent of the evanescent wave response reported in [16–18]. Fingerprints of a resonant behavior become perceptible for $Q \simeq 0.5$ with a shallow minimum of $\Im(Y)$ at $f \simeq f_0$ (figure 1(e)). A genuine resonance develops at $n \gtrsim 1 \times 10^{12} \text{ cm}^{-2}$ (figure 1(f)) and culminates at $f_0 \simeq 38$ GHz with $Q = 1.69$ for $n = 2 \times 10^{12} \text{ cm}^{-2}$ (figure 1(g)). We deduce a plasmon velocity $v_p = 4Lf_0 = 3.6 \times 10^6 \text{ m s}^{-1}$ in agreement with the above estimate based on geometry, and a plasmon damping length $\alpha^{-1} = (2Q/\pi)L \simeq 26 \mu\text{m}$. Plasmon losses correspond to a channel resistance $R = 40$ Ohms (figure 1(g)) approaching the characteristic impedance $Z_\infty = 35$ Ohms, which is a suitable measuring condition. The same procedure has been reproduced by recording 400 complex admittance spectra covering the density and temperature ranges, $n = -0.1$ – $2.25 \times 10^{12} \text{ cm}^{-2}$ and $T = 10$ – 300 K, where we find a quality factor peaking to $Q \gtrsim 2$ at 10 K (inset of figure 2(a)). Figures 2(a), (b) summarize the doping dependence of the resonator parameters $v_p(n)$, $Z_\infty(n)$ obtained using the same fitting procedure. From these values we calculate $\mathcal{L}_K(n)$, $\mathcal{C}(n)$ (30 K data in figure 2(c)) and find a good agreement with the theoretical capacitance formula (black dashed line), including the dip of $\mathcal{C}_Q(n)$ at neutrality. Still, we observe a deviation of $\mathcal{L}_K(n)$ from theory (blue dashed line) which exceeds our experimental uncertainties. This deviation is significant thanks to the increased accuracy of the resonant capacitor technique in the determination of \mathcal{C} and \mathcal{L}_K when compared to non-resonant techniques [7]. It is too large ($\gtrsim 100$ pH) to be explained by geometrical inductance effects ($\mu_0 W \sim 10$ pH) or systematic errors in the deembedding procedure (± 20 pH depending on frequency). From the channel resistance we estimate the conductivity and the mean free path $l_{mfp}(n, T)$ which is plotted in (figure 2(d)) for typical temperatures. Mobility saturates near $\mu = 250\,000 \text{ cm}^2 \text{ V}^{-1} \text{ s}^{-1}$ at low temperatures (dashed black line in figure 2(d)). At high temperatures we find a mean free path plateau $l_{mfp}(T) \sim 0.7 \times 300/T \mu\text{m}$, in agreement with theoretical estimates of the acoustic phonon limited resistivity [19].

To summarize, we have shown that the PRC principle works and provides an extensive characterization of equilibrium and transport graphene parameters including the compressibility $\mathcal{C}_Q(n, T)$, the kinetic inductance $\mathcal{L}_K(n, T)$ and the mean-free-path $l_{mfp}(n, T)$. The plasmon velocity matches expectations for the screened case. The weak doping dependencies of the plasmon velocity and characteristic impedance in figures 2(a), (b) reflect theoretical expectations for massless graphene where $v_p, Z_\infty \propto n^{-1/4}$ as opposed to $v_p \propto n^{-1/2}$ for massive 2DESs such as bilayer graphene. The deviation from theory, observed in the inductance, gives rise to a saturation of the plasmon velocity $v_p \lesssim 4v_F$ and characteristic impedance $Z_\infty \gtrsim 35$ Ohms. A tentative explanation for this discrepancy is an additive mass contribution from the dilute 2DES in the back-gated silicon substrate, which loads graphene Dirac plasmons according to its capacitive coupling to graphene electrons, and eventually restricts electron mobility. Such a residual substrate coupling can easily be avoided by substituting the silicon back gate with a metallic bottom gate following references [14, 20].

In conclusion, we have demonstrated a graphene PRC with a resonant frequency $f_0 \simeq 40$ GHz and a quality factor $Q \simeq 2$. Quality factors remain smaller than the $Q \sim 130$ reported in the ultrashort wavelength ($\lambda_p = 0.1$ – $0.2 \mu\text{m}$) MIR domain of [5]. However, the GHz damping length ($26 \mu\text{m}$) is comparable to the MIR value ($10 \mu\text{m}$ in [5]), which is promising for applications. We have measured the doping dependence of plasmon velocity, line capacitance and kinetic inductance in good agreement with theory beside a small shift of the kinetic inductance. Our experiment paves the way to active plasma resonance transistors working in the $0.1 \rightarrow 1$ THz domain, above the natural cutoff ~ 0.1 THz of conventional graphene field-effect transistors [21, 22]. Building on this first demonstration performed at cryogenic temperatures, a room temperature variant can be envisioned by scaling down the sample size and the plasmon wave length by a factor 10 to accommodate the phonon-limited mean free path of $0.7 \mu\text{m}$ at 300 K. During the reviewing process, we became aware of a related work [23] demonstrating the resonant detection of THz radiation using graphene plasmons. These achievements might in particular lead to the conception of novel detectors in the 600 GHz frequency domain, highly desirable for



air-craft RADARs operating in the mm-range, with a resolution ultimately limited by hot electron effects [14, 24, 25]. The long plasmonic channels are compatible with the incorporation of bottom gate arrays to engineer doping modulation profiles [26] and investigate the propagation of Dirac plasmons in bipolar superlattices.

Methods

Micromechanical exfoliation provides a pristine monolayer graphene, which is subsequently encapsulated between two layers of hexagonal boron nitride (hBN) in order to achieve a high electronic mobility (phonon limited at room temperature). The encapsulation is performed by means of a dry pick-up technique using a polyvinyl alcohol (PVA) and polymethylmethacrylate (PMMA) stamp on a polydimethylsiloxane support [8]. A top hBN flake (10–30 nm thick) is transferred from its substrate to the PMMA. Then the graphene is picked up by the first hBN flake thanks to the strong van der Waals interactions and deposited on a bottom hBN flake, which was previously exfoliated onto a high resistivity silicon (with SiO_2) substrate. The transfer process is carried out using a custom-made alignment system with a heating plate operating between 30 °C and 130 °C. Finally, the PVA and PMMA polymers are dissolved in hot water (95 °C) and acetone, respectively.

The encapsulated graphene samples are generally hundreds of μm^2 in size and need to be patterned into a passive circuit. After characterization by Raman spectroscopy (figure 3(c)) and atomic force microscopy (AFM, figure 3(a)), we used e-beam nanolithography to define a T-shape capacitor (figure 3(b)). The length of the channel, according to its mobility, defines the quarter wave plasma resonance and needs to be long enough to obtain a signal in the

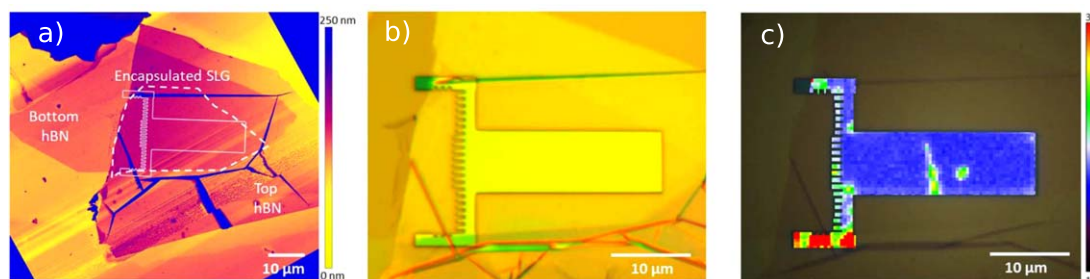


Figure 3. Fabrication process of a plasma resonance capacitor (PRC). (a) AFM image of the hBN/graphene/hBN stack deposited on the high-resistivity SiO₂/Si substrate. The dashed and solid lines show the contours of the pristine graphene flake and targeted PRC sample. (b) Optical image of the PRC sample after lithography, before etching. (c) Map of the Raman 2D-peak width (color encoded in the range 10–30 cm⁻¹) showing the good sample homogeneity and highlighting the presence of a spurious fold and bubble in this sample (PRC7).












0–40 GHz bandwidth. The etching of the hBN-graphene-hBN sandwich was performed using a mixture of CHF₃/O₂ plasma etching through a temporary 40 nm thick aluminum mask. A chromium/gold (5/200 nm) edge contact was then deposited on the source edge of the T-shape heterostructures (using a comb design to enhance the contact length and reduce the contact resistance). In order to passivate the other edges of the heterostructures and to avoid any source-gate leakage current in the PRC, we oxidized 2 nm of aluminum followed by 10 nm of Al₂O₃ by atomic layer deposition. Finally, a chromium/gold gate electrode was deposited on top and the PRC was embedded into a CPW. Similarly, thru-line and dummy reference structures were defined on the same chip for de-embedding (see below).

High frequency admittance measurements were carried out in a Janis cryogenic probe station in the temperature range $T = 10\text{--}300$ K. The two-port scattering parameters S_{ij} of the capacitor were measured using an Anritsu MS4644B VNA in the 0–40 GHz range. Bias tees were used to decouple the DC gate voltages from the GHz probe signal. A short-open-load-reciprocal protocol was used to calibrate the wave propagation until the probe tips. We then measured S parameters of a symmetric thru-line reference structure, calculated its $ABCD$ (cascade) matrix A_{thru} , and took the inverse of the square root of this matrix $A_{thru}^{-1/2}$. The wave propagation in the coplanar access of the PRC can now be de-embedded from its $ABCD$ matrix: $A_{PRC}^{deem} = A_{thru}^{-1/2} \cdot A_{PRC} \cdot A_{thru}^{-1/2}$. The same procedure was carried out on a dummy reference structure which has the same contact and gate geometry as the PRC but does not contain encapsulated graphene. Finally, the $ABCD$ matrices of the PRC and the dummy structure were converted to admittance (Y) parameters and the Y matrix of the dummy structure was subtracted from that of the PRC in order to de-embed remaining stray capacitances. The Y_{ij} parameters should now all be the same (except for a minus sign in front of the off-diagonal elements), due to the symmetry of our two-port network. The admittance data shown in this article correspond to one of the off-diagonal elements, $-Y_{12}$, which was further de-embedded from the contact resistance: $Y = (-1/Y_{12} - R_c)^{-1}$.

Acknowledgments

The research leading to these results has received partial funding from the the European Union ‘Horizon 2020’ research and innovation programme under grant agreement No. 785219 ‘Graphene Core’, and from the ANR-14-CE08-018-05 ‘GoBN’.

ORCID iDs

H Graef  <https://orcid.org/0000-0002-2531-1775>
 D Mele  <https://orcid.org/0000-0002-2250-9671>
 L Banszerus  <https://orcid.org/0000-0002-1855-1287>
 C Stampfer  <https://orcid.org/0000-0002-4958-7362>
 T Taniguchi  <https://orcid.org/0000-0002-1467-3105>
 K Watanabe  <https://orcid.org/0000-0003-3701-8119>
 E Bocquillon  <https://orcid.org/0000-0002-5875-1718>
 G Fève  <https://orcid.org/0000-0001-5587-7537>
 J-M Berroir  <https://orcid.org/0000-0001-7344-0929>
 E H T Teo  <https://orcid.org/0000-0003-0528-1764>
 B Plaçais  <https://orcid.org/0000-0003-2408-7393>

References

- [1] Das Sarma S, Adam S, Hwang E H and Rossi E 2011 Electronic transport in two-dimensional graphene *Rev. Mod. Phys.* **83** 407
- [2] Burke P J, Spielman I B, Eisenstein J P, Pfeiffer L N and West K W 2000 High frequency conductivity of the high-mobility two-dimensional electron gas *App. Phys. Lett.* **76** 745
- [3] Grigorenko A N, Polini M and Novoselov K S 2012 Graphene plasmonics *Nat. Photon.* **6** 749
- [4] Lundberg M B *et al* 2017 Tuning quantum nonlocal effects in graphene plasmonics *Science* **357** 187
- [5] Ni G X *et al* 2018 Fundamental limits to graphene plasmonics *Nature* **557** 530
- [6] Knap W, Deng Y, Rumyantsev S and Shur M S 2002 Resonant detection of subterahertz and terahertz radiation by plasma waves in submicron field-effect transistors *Appl. Phys. Lett.* **81** 4637
- [7] Yoon H, Forsythe C, Wang L, Tombros N, Watanabe K, Taniguchi T, Hone J, Kim P and Ham D 2014 Measurement of collective dynamical mass of Dirac fermions in graphene *Nat. Nanotechnol.* **9** 594
- [8] Banszerus L, Schmitz M, Engels S, Goldsche M, Watanabe K, Taniguchi T, Beschoten B and Stampfer C 2016 Ballistic transport exceeding 28 μm in CVD grown graphene *Nano Lett.* **16** 1387
- [9] Ryzhii V, Otsuji T, Ryzhii M and Shur M S 2012 Double graphene-layer plasma resonances terahertz detector *J. Phys. D: Appl. Phys.* **45** 302001
- [10] Aizin G R and Dyer G C 2012 Transmission line theory of collective plasma excitations in periodic two-dimensional electron systems: Finite plasmonic crystals and Tamm states *Phys. Rev. B* **86** 235316
- [11] Bandurin D A *et al* 2016 Negative local resistance caused by viscous electron backflow in graphene *Science* **351** 1055
- [12] Crossno J *et al* 2016 Observation of the Dirac fluid and the breakdown of the Wiedemann–Franz law in graphene *Science* **351** 1058
- [13] Tielrooij K-J *et al* 2018 Out-of-plane heat transfer in van der Waals stacks through electron-hyperbolic phonon coupling *Nat. Nanotechnol.* **13** 41
- [14] Yang W *et al* 2018 A graphene Zener–Klein transistor cooled by a hyperbolic substrate *Nat. Nanotechnol.* **13** 47
- [15] Chaste J, Lechner L, Morfin P, Fève G, Kontos T, Berroir J-M, Glatli D C, Happy H, Hakonen P and Plaçais B 2008 Single carbon nanotube transistor at GHz frequency *Nano Lett.* **8** 525
- [16] Pallecchi E, Betz A C, Chaste J, Fève G, Huard B, Kontos T, Berroir J-M and Plaçais B 2011 Transport scattering time probed through rf admittance of a graphene capacitor *Phys. Rev. B* **83** 125408
- [17] Inhofer A *et al* 2017 Observation of Volkov–Pankratov states in topological HgTe heterojunctions using high-frequency compressibility *Phys. Rev. B* **96** 195104
- [18] Inhofer A *et al* 2018 RF-quantum capacitance of topological insulator Bi_2Se_3 in the bulk depleted regime for field-effect transistors *Phys. Rev. Appl.* **9** 024022
- [19] Hwang E H and Das Sarma S 2008 Acoustic phonon scattering limited carrier mobility in two-dimensional extrinsic graphene *Phys. Rev. B* **77** 115449
- [20] Wilmart Q, Inhofer A, Boukhicha M, Yang W, Rosticher M, Morfin P, Garroum N, Fève G, Berroir J-M and Plaçais B 2016 Contact gating at GHz frequency in graphene *Sci. Rep.* **6** 21085
- [21] Pallecchi E, Benz C, Betz A C, Löhneysen H v, Plaçais B and Danneau R 2011 Graphene microwave transistors on sapphire substrates *Appl. Phys. Lett.* **99** 113502
- [22] Mele D, Mehdhbi S, Fadil D, Wei W, Ouerghi A, Lepilliet S, Happy H and Pallecchi E 2018 Graphene FETs based on high resolution nanoribbons for HF low power applications *Electron. Mater. Lett.* **14** 133
- [23] Bandurin D A *et al* 2018 Resonant terahertz detection using graphene plasmons (arXiv:1807.04703)
- [24] Betz A C *et al* 2012 Hot electron cooling by acoustic phonons in graphene *Phys. Rev. Lett.* **109** 056805
- [25] Betz A C *et al* 2013 Supercollision cooling in undoped graphene *Nat. Phys.* **9** 109–112
- [26] Wilmart Q, Berrada S, Torrin D, Nguyen V H, Fève G, Berroir J-M, Dollfus P and Plaçais B 2014 A Klein-tunneling transistor with ballistic graphene *2D Mater.* **1** 011006